

This is the Author's Pre-print version of the following article: *C.O. Aguilar-Ortiz, D. Soto-Parra, P. Álvarez-Alonso, P. Lázpita, D. Salazar, P.O. Castillo-Villa, H. Flores-Zúñiga, V.A. Chernenko, Influence of Fe doping and magnetic field on martensitic transition in Ni–Mn–Sn melt-spun ribbons, Acta Materialia, Volume 107, 2016, Pages 9-16*, which has been published in final form at <https://doi.org/10.1016/j.actamat.2016.01.041> This article may be used for non-commercial purposes in accordance with Terms and Conditions for Self-Archiving

Influence of Fe doping and magnetic field on martensitic transition in Ni-Mn-Sn melt-spun ribbons

C.O. Aguilar-Ortiz^a, D. Soto-Parra^a, P. Álvarez-Alonso^b, P. Lázpita^b, D. Salazar^c, P.O. Castillo-Villa^a, H. Flores-Zúñiga^a,
V.A. Chernenko^{c,d}

^a *División de Materiales Avanzados, Instituto Potosino de Investigación Científica y Tecnológica A.C., San Luis Potosí 78216, Mexico*

^b *Departamento de Electricidad y Electrónica, Universidad del País Vasco (UPV/EHU), Leioa 48940, Spain*

^c *BCMaterials & University of Basque Country (UPV/EHU), Bilbao 48080, Spain*

^d *Ikerbasque, Basque Foundation for Science, Bilbao 48013, Spain*

Abstract

Mn-rich Ni-Mn-Sn metamagnetic shape memory alloys exhibiting magnetostructural transformation are of a great potential as the base materials for solid-state refrigeration. With the aim of fine tuning of the transformation characteristics and improving functional properties, in the present work we have fabricated polycrystalline $\text{Ni}_{50-x}\text{Fe}_x\text{Mn}_{40}\text{Sn}_{10}$ ($x = 0, 2, 4, 6, 8$ at.%) melt-spun ribbons, starting from the base alloy with $x = 0$, which is weakly magnetic in both austenitic and martensitic phases. By exploring martensitic transformation (MT) and magnetic behaviors as a function of Fe doping and magnetic field, we have found that Fe and/or magnetic field reduces the MT temperature and Curie temperature of austenite phase, making them closer to each other as the Fe-content increases, accompanied by a sharp increase of the magnetic moment of austenite, magnetization jump at MT, transformation volume and magnetic contribution, ΔS_M , to the total entropy change at MT. The proximity of the MT and Curie temperatures reduces the refrigerant capacity of the second-order magnetic phase transition but keeps unaltered that of the structural transition. The ribbons are promising for the ambient magnetocaloric and elastocaloric cooling applications because of an appropriate shape for the heat exchange, moderate values of ΔS_M equal to $11 \text{ J kg}^{-1}\text{K}^{-1}$ at 5 T for $x = 8$, small thermal hysteresis (5 -10 K) nearly independent of Fe doping or magnetic field, and adjustable structural and magnetic transition temperatures close to room temperature.

Keywords: martensitic transformation; phase diagram; entropy; transformation volume; magnetocaloric effect.

1. Introduction

Ferromagnetic shape memory alloys (FSMAs) are mostly off-stoichiometric Heusler type materials that have attracted much attention due their potential use in many applications, particularly since

some alloys of the Ni-Mn-Ga system have shown a giant magnetic-field-induced strain, associated to the reorientation of the martensitic microstructure [1–4]. Recently, the Mn-rich Ni-Mn-X (X = In, Sn, and Sb) Heusler-type compounds, the so-called metamagnetic shape memory alloys (MetaMSMAs), have stood out due to their remarkable properties such as giant caloric effects [5–11] and easy-tunable transformation characteristics by a variation of the composition and doping [12–16]. Particularly, in the case of Ni-Mn-Sn MetaMSMAs, a fourth element addition normally seeks to improve the magnetic properties although it can also modify the structure. A Co doping of $\text{Ni}_{50-x}\text{Co}_x\text{Mn}_{38}\text{Sn}_{12}$ increases the Curie temperature of austenite, T_C^A [17]. The Ni substitution by 1 at.% Co or 3 at.% Fe in $\text{Ni}_{49.9}\text{Mn}_{37.1}\text{Sn}_{13.0}$ increases the martensitic temperatures as well as the magnetocaloric effect: the entropy change for 3 at.% Fe reaches $30 \text{ Jkg}^{-1}\text{K}^{-1}$ at $\mu_0\Delta H = 5\text{T}$, much larger than $20 \text{ Jkg}^{-1}\text{K}^{-1}$ obtained in the ternary counterpart [18]. Substituting Mn by Fe in $\text{Ni}_{50}\text{Mn}_{37-x}\text{Fe}_x\text{Sn}_{13}$ and $\text{Ni}_{50}\text{Mn}_{36-x}\text{Fe}_x\text{Sn}_{14}$ alloys enlarges T_C^A [19,20]. A similar behavior is observed in $\text{Ni}_{50}\text{Mn}_{40-x}\text{Fe}_x\text{Sn}_{10}$, but a replacement of Mn by Fe above 3 at.% leads to the precipitation of a second phase (Fe-enriched γ -phase) accompanied by a decrease of the martensitic temperatures [21].

Rapid solidification by the melt spinning technique implies several advantages for the fabrication of MetaMSMAs. It has been used to obtain the homogeneous, chemically ordered and single phase polycrystalline ribbons of the Ni-Mn-Sn alloys [22,23] without a need for the additional heat treatment [24] at 1173 K for two days used in the bulk [19]. Moreover, this technique facilitates the formation of textured samples with improved mechanical properties. This fabrication method is well suited for developing of the magnetocaloric materials because the geometry of the ribbons (large surface area along the ribbon length with a ribbon thickness of few microns) ensures a fast heat exchange with the heat transfer fluid in a magnetocaloric device [25]. In this sense, several magnetocaloric materials have been synthesized in the ribbon form [26–28]. Alongside magnetic refrigeration, the ribbons of these compounds could be used as the rapid magnetic actuators, e.g., in the automotive applications. Note that the transformation temperatures close to room temperature and low magnetic field required for the actuation are the key parameters for practical use of MetaMSMAs.

In this work, we systematically studied the influence of the Ni substitution by Fe and magnetic field on the structure, phase transition, and magnetocaloric properties of the $\text{Ni}_{50}\text{Mn}_{40}\text{Sn}_{10}$ MetaMSMAs melt-spun ribbons. Particularly, the interrelationship between the transformation volume, magnetization jump, and entropy change is experimentally explored.

2. Experimental

Polycrystalline $\text{Ni}_{50-x}\text{Fe}_x\text{Mn}_{40}\text{Sn}_{10}$ ($x = 0, 2, 4, 6, 8$) alloys were prepared by arc melting from high purity metals ($> 99.9\%$) in argon atmosphere. The alloys were re-melted several times to improve homogeneity. Melt-spun ribbons were obtained from the as-cast ingots at a wheel linear speed of 35 m/s under Ar pressure. The ribbons were 1-2 mm wide and 10-20 μm thick.

Microstructure was examined at room temperature by a scanning electron microscope (SEM) FEI-Helios Nanolab 600. The chemical composition was analyzed by a Hitachi TM3000 SEM equipped with an energy dispersive X-ray spectroscopy (EDS) system. Table 1 shows a concordance between the actual and nominal compositions.

Martensitic transformation (MT) temperatures and transformation enthalpies were determined by differential scanning calorimetry (DSC) using a TA-Instruments model Q200 at cooling/heating rate of 10 K/min. Crystal structures and lattice parameters were studied by X-ray diffraction (XRD) in the temperature range from 277 K to 465 K with a heating rate of 0.2 K s^{-1} in a Bruker D8 Advance diffractometer (30 kV and 20 mA, $\lambda_{\text{Cu}} = 1.5418\text{ \AA}$). Le Bail analysis of the diffraction data was carried out with the FullProf suite [29]. The lattice parameters of martensite structure were determined by means of a traditional refinement using X-ray measurements of the samples with NaCl powder, the latter data were used to fix the zero displacement. The results appeared self-consistent within $\pm 0.02\text{ \AA}$.

The temperature dependences of electric resistance were recorded by a four-terminal method with a temperature step of 3 K. The thermomagnetization, $M(T)$, measurements were carried out using both a customary made 1.9 T vibrating sample magnetometer (VSM) operating up to 670 K and a Quantum Design PPMS ® Evercool-I 9T platform with the upper temperature limit of 400 K. Magnetic field, $\mu_0 H$, was applied along the ribbon length to minimize a demagnetizing field effect. The characteristic temperatures of MT and Curie temperatures have been extracted from the DSC and $M(T)$ dependences, respectively, by a conventional tangential method.

3. Results

3.1. Microstructure

Fig. 1 and insets show typical SEM micrographs of the surface and fracture cross-section of the $\text{Ni}_{50.3}\text{Mn}_{39.7}\text{Sn}_{9.9}$ and $\text{Ni}_{48.5}\text{Mn}_{39.5}\text{Sn}_{9.8}\text{Fe}_{2.2}$ as-spun ribbons. All ribbons are well-crystallized and

demonstrate a columnar grain structure across the ribbon thickness. They exhibit a diversity of the grain shapes and sizes ranging from 1 to 10 μm , the characteristics typical for ribbons fabricated by melt spinning [27]. The average grain size in the ternary alloy is few times larger than the one in Fe doped counterparts. Besides, a two-twin-variants pattern of the martensitic substructure appears well-pronounced inside of each grain. A similar martensitic structure including certain porosity, with the pore sizes below 1 μm , were observed for the other ribbons studied in this work. The secondary electron SEM images of the ribbon cross-sections (see a representative image for $\text{Ni}_{48.5}\text{Mn}_{39.5}\text{Sn}_{9.8}\text{Fe}_{2.2}$ in the inset of Fig. 1(b)) evidence an absence of second phase, unlike the case of the bulks with similar composition produced by conventional arc melting, which exhibit γ - phase precipitates [21].

3.2. Martensitic transformation

Figs. 2(a) and (b) display the DSC thermograms and the temperature dependences of electric resistance, $R(T)$, in the vicinity of MT temperatures of the ribbons. The data show sharp anomalies produced by MT accompanied by a small thermal hysteresis, which varies between 5 K and 10 K. Such behavior reflects a high homogeneity and one-phase state of the ribbons despite no heat treatment has been carried out. The exothermic and endothermic peaks on DSC profiles served for the determination of the MT temperatures and transformation enthalpies, which are summarized in Table 1. Fe doping leads to a monotonous dependence of the values of the start and finish martensitic (T_{MS} , T_{MF}) and austenitic (T_{AS} , T_{AF}) transformation temperatures as well as the averaged for the forward and reverse MT enthalpies, $|\Delta H|$. Note that the characteristic temperatures for the ribbon of ternary alloy are in line with those of the bulk alloys with similar composition [13,30]. Some mismatch in the transformation temperatures between the DSC and resistance data in Fig. 2(a,b) is attributed to the different environmental conditions of the samples during heating/cooling ramps in each case. The large change of resistance at MT together with its very steep temperature dependence and narrow hysteresis are the preconditions for a reversible giant magnetoresistance effect in the vicinity of MT in the ribbons, representing one of the important functional characteristics of MetaMSMAs (see, e.g., [31]).

Fig. 3 shows typical XRD patterns for the $\text{Ni}_{48.5}\text{Mn}_{39.5}\text{Sn}_{9.8}\text{Fe}_{2.2}$ ribbon recorded at different constant temperatures across MT during step-wise heating. Note the extinction of the former and appearance of new diffraction peaks in the temperature range of MT; this temperature range agrees with the DSC results. The fits in Figs. 3 (a) and (b) evidence that the peaks above T_{AF} and below T_{AS} are well-indexed in terms of a cubic $\text{Pm}\bar{3}\text{m}$ austenite and orthorhombic 7M modulated martensite,

respectively. A similar martensitic structure has been observed in Ref. [32]. The presence of the (200) reflection at $2\theta \approx 30^\circ$ in the cubic phase indicates a B2 atomic order between the nearest neighbors in the BCC lattice. At the temperatures between T_{AS} and T_{AF} , the martensitic and austenitic phases coexist. No second phase is detected, in agreement with the microstructural observations.

Fig. 4 represents the temperature dependences of the lattice parameters for all the ribbons. The continuous enlargement of the parameters for austenite and orthorhombic martensite with temperature corresponds to the normal thermal expansion observed in the common metals. According to Fig. 4d, a substitution of Ni by Fe systematically increases the lattice parameter of austenite, a_0 , as it does with the martensitic lattice parameter, c , whereas the lattice parameters a and b do not exhibit essential changes (cf. Ref. [20]).

3.3. Magnetic properties

Fig. 5 depicts the low-field magnetization as a function of temperature for the Fe doped ribbons measured by PPMS using the zero-field-cooled (ZFC) and field-cooled (FC) protocol (i.e., for ZFC, the sample was initially cooled in zero-magnetic field and then the data were collected on warming at a magnetic field of 5 mT. For FC, the data were acquired on cooling at 5 mT). Much less sensitive than PPMS, our VSM was used at applied field of 0.5 T to detect transformations anomalies in a ternary alloy, which is hardly magnetic at 5 mT in the entire temperature range including MT range above 400 K (see Inset in the bottom panel of Fig. 5). The $M(T)$ graphs in Fig. 5 and Insets demonstrate many interesting features and trends as a function of Fe doping. Particularly, the curves show hysteretic anomalies related to MT. The values of the start (T_{MS} , T_{AS}) and finish (T_{MF} , T_{AF}) MT temperatures, determined by a tangent method, agree with the data of the calorimetric measurements. Fig. 5 and Insets show that, during cooling, the paramagnetic austenite starts to exhibit a ferromagnetic ordering at the Curie temperature of austenite, T_C^A , shortly interrupted by MT with the formation of an almost non-magnetic martensite. After further cooling, it commences to show some ferromagnetic ordering process at T_C^M (tentatively called Curie temperature of martensite). Table 1 summarizes the martensitic and austenitic Curie temperatures determined from the analysis of $M(T)$ curves in Fig.5. While the values of T_C^M indicated in Fig. 5 are easy to determine by a tangent method, this is not the case with the values of T_C^A due to the temperature limit of PPMS. In the last case, we use $M(T)$ anomaly for ribbon with $x = 6$ shifting it along x -axis until matching with the parts of the same anomalies for the other ribbons.

Below T_C^M , the ZFC and FC curves split, indicating an irreversible magnetic phenomena related to the domain wall freezing that have been observed in the bulk Ni-Mn-Sn [30,33,34]. The ZFC curves

show a rapid increment of the magnetization from low temperatures to the blocking temperature, T_B , (tentatively defined as the temperature at which the magnetization of the ZFC reaches a maximum). Such behavior has been linked to the presence of antiferromagnetic coupling that pins the ferromagnetic matrix in different spin configurations depending on the applied magnetic field, whereby promoting an exchange bias effect in Ni-Mn-Sn alloys [35].

The magnetic field influence on the transformation behavior of the ribbons, except of the one with $x = 0$, is demonstrated in Fig. 6 by the selected $M(T)$ curves recorded by using FC procedure. For the sake of clarity, only heating dependences are shown. Since the magnetic field shifts the MT temperature downward faster than austenitic Curie temperature (cf. Ref. [8]), a considerable increase of the magnetization jump, ΔM , (defined as the difference between the magnetization at the upper and lower bounds of the abrupt change) is observed. It follows from Figs. 5 and 6 that Fe doping appears more effective to reduce the MT temperature and to increase ΔM than the magnetic field, despite some concomitant decrease of T_C^A . For example, the magnetization jump for the ribbon with $x = 8$ is about 46 % larger than for the one with $x = 6$. The absolute values of the magnetization in both martensite and austenite are strongly influenced by the amount of Fe content (Fig. 5) and magnetic field (Fig. 6).

4. Discussion

In the present work, we found that Fe doping up to 8 at.% instead of Ni in $\text{Ni}_{50}\text{Mn}_{40}\text{Sn}_{10}$ alloy neither leads to the formation of second phase nor modifies the crystal structure of martensite. The latter fact allows considering the influence of Fe on the transformation behavior and magnetic properties of this compound in terms of the volume and valence electron concentration, e/a , effects, representing main factors controlling structural and magnetic instabilities in the Hume-Rothery alloys [36].

Fig. 4 demonstrates that Fe doping increases the lattice parameter of cubic austenite and parameter c of orthorhombic martensite with no essential changes in the parameters a and b . The almost linear increase is expected according to the Vegard's law since the atomic radius of Fe is larger than Ni by 0.08\AA [37].

The temperature dependence of the lattice unit cell volume for each ribbon depicted in Fig. 7, where $V_A(T)$ and $V_M(T)$ stand for austenite and martensite, respectively, was calculated using data in Fig. 4. From the linear fits, the experimental values of transformation volume, $\Delta V/V = (V_A - V_M)/V_M$, at selected temperatures $T_1 \approx T_A = (T_{AF} + T_{AS})/2$, taken at the middle point of the gap between

extrapolated $V_A(T)$ and $V_M(T)$ dependencies as shown in Fig. 7, were obtained for each ribbon and collected in Table 1.

Both thermodynamic characteristics of MT, such as the transformation entropy change (calculated using enthalpies from Table 1) and experimental $\Delta V/V$, are plotted in Fig. 8(a) as a function of Fe content.

The phase diagram of the martensitic and magnetic transitions in the studied alloys is shown in Fig. 8(b). Replacing Ni by Fe in $\text{Ni}_{50}\text{Mn}_{40}\text{Sn}_{10}$ causes a strong linear decrease of both the T_C^A and quasi-equilibrium MT temperature, $T_0 = (T_A + T_M)/2$, (~ 17 K/Fe at.% for T_0) accompanied by a moderate increase of the entropy, ΔS^{MT} , and volume, $\Delta V/V$, changes at MT (Fig. 8(a,b)), alongside a considerable increase of the magnetization jumps, ΔM (Fig. 6). Thus, one can conclude that Fe doping enforces a first-order character of MT in the studied ribbons. Whereas the mentioned shift of T_0 downwards correlates with a decrease of e/a ratio (see Table 1), which is in line with the well-known e/a -tendency in NiMn-based Heusler alloys (see, e.g., Refs. [36,38]), this is not the case for T_C^A . Since it is known that the hydrostatic pressure increases the Curie temperature in NiMn-based Heusler alloys [39,40], one should recognize that the controlling factor in the observed reduction of T_C^A would be a Fe-induced expansion of the specific volume of the austenite phase (Fig. 7). This suggests that the Ni substitution by Fe reduces the volume dependent spin exchange interactions between the Mn atoms in austenite. The Table 1 and Fig. 8(b) evidence that T_C^M is almost insensitive to the Fe doping which, taking into account its much steeper e/a dependence in the martensitic state [38], can be reasonably explained by a nearly compensated mutual influence of e/a and volume factors.

It is worth noting that the phase diagram in Fig. 8(b) indicates a very close positions of the T_C^A and T_0 becoming even closer as a function of the Fe doping. Moreover, this behavior is observed in a broad temperature range (~ 140 K), which is appealing for applications as it is associated with a pronounced magnetocaloric effect. The closeness of T_C^A and T_0 , which particularly implies larger magnetic entropy contribution to the total entropy change at MT (see discussion below and Ref. [41]), together with the large magnetization change observed in the $M(T)$ curves (see Fig. 6), provide necessary conditions for a noticeable magnetic field-induced entropy change, ΔS_M , in the studied ribbons.

We calculated the temperature dependence of ΔS_M from the $M(T)$ curves at different applied magnetic fields shown in Fig. 6 using the Maxwell relationship [5]. Fig. 9(a) depicts the magnetic entropy change as a function of temperature under different applied magnetic field changes ($\mu_0\Delta H = 1, 2, 3, \text{ and } 5$ T). Each curve presents two peaks: the positive one at lower temperature, characterized

by a high and narrow maximum, results from the change of the magnetic structure due to the first-order reverse MT from the weakly magnetic martensitic phase to the ferromagnetic austenitic structure, whereas the negative one, a broad minimum characteristic of a second-order magnetic phase transition, corresponds to the ferromagnetic phase transition in the austenite phase. These peaks represent the inverse (IMCE) and conventional (MCE) magnetocaloric effects respectively [7,8]. In the studied ribbons, IMCE is about four times larger than MCE, Fig. 9(a). Fig. 9(b) shows the maxima of magnetic entropy change (ΔS_M^{Max}) as a function of the magnetic field change for ribbons with $x = 2, 4, 6,$ and 8 . The peak values increase with the magnetic field and Fe doping. The latter behavior differs from the one reported for a $\text{Ni}_{46-x}\text{Fe}_x\text{Mn}_{43}\text{Sn}_{11}$ ($x = 0, 1, 2, 3$) as-spun ribbons, where ΔS_M^{Max} for the ternary alloy reaches $21.0 \text{ J kg}^{-1}\text{K}^{-1}$ at $\mu_0\Delta H = 5 \text{ T}$ but Fe doping produces highly irregular up-and-down dependence for ΔS_M^{Max} with the final value of $14.8 \text{ J kg}^{-1}\text{K}^{-1}$ for 3 Fe at.% [34]. In our study, the ribbons with 8 at.% Fe present the highest value of the magnetic entropy change for IMCE, $\Delta S_M = 11.0 \text{ J kg}^{-1}\text{K}^{-1}$ at 5 T. It is worth mentioning that the maximum of the magnetic entropy change moves to lower temperatures under magnetic field due to the shift of the MT temperature.

Fig. 9(c) represents the phase diagrams ‘MT temperature versus applied magnetic field’ for ribbons. The dependences are quasi-linear (regression coefficient ~ 0.9) with the slopes increasing during Fe doping from -0.06 to -0.95 KT^{-1} . The slope of $\sim -1 \text{ KT}^{-1}$ has been observed in ternary Ni-Mn-Sn alloys [8]. This parameter together with the value of temperature hysteresis of MT are considered as the important factors determining a ‘temperature - magnetic field’ window for the magnetocaloric operations [42].

Another important figure of merit to characterize magnetocaloric effect of a given material is the refrigerant capacity such as the relative cooling power, RCP, defined as an area under the $\Delta S_M(T)$ curves, using the temperatures at half maximum of the peak as the numerical integration limits [43].

Fig. 10 depicts the magnetic field influence on RCP associated with IMCE at MT in the ribbons. The inset in Fig. 10 plots RCP produced by a conventional MCE during the ferromagnetic ordering of austenite in the ribbons with $x = 6$ and 8 (instrumental limitations did not allow to reach the full width at half maximum for $x = 2$ and 4). The RCP values related to both the first-order MT and the second order ferromagnetic transition increase with the Fe content reflecting an effect of enlargement of ΔS_M with the Fe doping. The RCP at $\mu_0\Delta H = 5 \text{ T}$ for IMCE reaches 9, 11, 45, and 82 J kg^{-1} at $x = 2, 4, 6,$ and 8 Fe at.% respectively, whereas RCP values for MCE are 31 J kg^{-1} and 67 J kg^{-1} for ribbons with 6 and 8 Fe at.%, respectively. Note that, due to the proximity between the structural and

magnetic transitions, the full width at half maximum of the ΔS_M peak for the ferromagnetic transition is strongly reduced whereas ΔS_M associated with MT is hardly affected.

The total entropy change during MT, ΔS^{MT} , comprises the magnetic and vibrational contributions. Recently, the total entropy has been empirically and theoretically related to the difference between the austenite Curie temperature and martensitic transformation temperature, showing that those materials with a small positive value of $(T_C - T_0)$, exhibit the largest ΔS^{MT} , which exponentially decreases as $(T_C - T_0)$ increases [44,45]. Such behavior is explained by a reduction of the magnetic contribution [46]. The generalized order parameter $(T_C - T_0)$ can be varied by the alloy composition, degree of atomic order and/or magnetic field (see [46,47] and references therein). Fig. 11 shows the experimental results of the total transformation entropy ΔS^{MT} versus $(T_C^A - T_0)$, obtained from DSC measurements of the studied ribbons and the data for other NiMn-based Heusler metamagnetic materials from the literature. All the data have been fitted by one universal exponential dependence. Note that the total entropy of martensitic transformation grows as Ni is substituted by Fe (equivalently, T_C^A and T_0 become closer). In contrast, the total entropy decreases when Mn is replaced by Fe [21].

Substituting Ni by Fe in Ni-Mn-Sn alloys maintains the difference between the vibrational entropies of the austenite and martensite phases unaltered for low Fe content as the structures are fixed and transformation volume variation is relatively weak. Therefore, higher values of ΔS^{MT} in ribbons with bigger amount of Fe are associated with an increase of the magnetic entropy contribution to the total entropy change, which is in agreement with the global dependence shown in Fig.11. These data suggest that magnetic contribution is the main reason of both MCE and IMCE phenomena in the studied alloys.

5. Summary

In the present work, we show that the polycrystalline as-spun ribbons of $Ni_{50-x}Fe_xMn_{40}Sn_{10}$ ($x = 0, 2, 4, 6, \text{ and } 8$) metamagnetic shape memory alloys exhibit MT from weakly magnetic orthorhombic 7M martensitic phase to a ferromagnetic cubic austenite with a thermal hysteresis 5-10 K. The important detail is that the master alloy with $x = 0$ is weakly magnetic not only in the martensitic but also in the austenitic phase. The progressive substitution of Ni by Fe increases both the austenite and martensite unit cell volumes, as well as tends to increase the transformation volume, $\Delta V/V$, above 1%. Furthermore, the Fe doping causes increasing of the transformation entropy. Both the Fe doping and

magnetic field drastically increase the magnetization jumps at MT, whereas the MT temperatures exhibit a moderate linear decrease. The calculated magnetic entropy change presents two peaks associated with the martensitic and ferromagnetic transitions; for a magnetic field change of 5 T, the maximum value (related to inverse magnetocaloric effect at MT) is $11.0 \text{ J kg}^{-1} \text{ K}^{-1}$ for ribbon with $x = 8$. The Relative Cooling Power is lower for the ferromagnetic phase transition in austenite ($\text{RCP} = 82$ and 66 J kg^{-1} at $\mu_0 \Delta H = 5 \text{ T}$ for the structural and magnetic transitions respectively, in the ribbon with $x = 8$) due to the proximity of the martensitic and magnetic phase transformations. Fe doping increases the magnetic contribution to the total entropy change at MT. Generally, we have found that Fe doping allows a fine-tuning of the transformation and magnetocaloric behavior of the studied ribbons. The ribbons with $x = 6$ or 8 can serve as magnetocaloric or elastocaloric materials for possible applications in prototype devices for solid state refrigeration.

Acknowledgements

This work was supported by the Mexican CONACYT (project CB-157541), the Spanish Ministry of Economy and Competitiveness (project MAT2014-56116-C4-3-4-R), the Basque Government (IT711-13), and University of Basque Country, UPV/EHU, (EHUA13/22). Authors thank technical support of Dr. G.J. Labrada, M.Sc. A.I. Peña, M.Sc. B. Rivera for SEM, XRD at LINAN laboratory in IPICYT and of J.L. Sánchez-Llamazares for magnetic measurements in a PPMS VSM in IPICYT. Technical and human support provided by SGIker (UPV/EHU, GV/EJ, ESF) is gratefully acknowledged.

References

- [1] K. Ullakko, J.K. Huang, C. Kantner, R.C. O'Handley, V.V. Kokorin, Large magnetic-field-induced strains in Ni₂MnGa single crystals, *Appl. Phys. Lett.* 69 (1996) 1966–1968.
- [2] S.J. Murray, M. Marioni, S.M. Allen, R.C. O'Handley, T.A. Lograsso, 6% magnetic-field-induced strain by twin-boundary motion in ferromagnetic Ni–Mn–Ga, *Appl. Phys. Lett.* 77 (2000) 886–888.
- [3] A. Sozinov, A.A. Likhachev, N. Lanska, K. Ullakko, Giant magnetic-field-induced strain in NiMnGa seven-layered martensitic phase, *Appl. Phys. Lett.* 80 (2002) 1746–1748.
- [4] R. Kainuma, Y. Imano, W. Ito, Y. Sutou, H. Morito, S. Okamoto, O. Kitakami, K. Oikawa, A. Fujita, T. Kanomata, K. Ishida, Magnetic-field-induced shape recovery by reverse phase transformation, *Nature*. 439 (2006) 957–960.
- [5] T. Krenke, E. Duman, M. Acet, E.F. Wassermann, X. Moya, L. Mañosa, A. Planes, Inverse magnetocaloric effect in ferromagnetic Ni–Mn–Sn alloys, *Nat. Mater.* 4 (2005) 450–454.
- [6] Z.D. Han, D.H. Wang, C.L. Zhang, S.L. Tang, B.X. Gu, Y.W. Du, Large magnetic entropy changes in the Ni_{45.4}Mn_{41.5}In_{13.1} ferromagnetic shape memory alloy, *Appl. Phys. Lett.* 89 (2006) 182507.
- [7] L. Mañosa, D. González-Alonso, A. Planes, E. Bonnot, M. Barrio, J.-L. Tamarit, S. Aksoy, M. Acet, Giant solid-state barocaloric effect in the Ni–Mn–In magnetic shape-memory alloy, *Nat. Mater.* 9 (2010) 478–481.
- [8] V.A. Chernenko, J.M. Barandiarán, J. Rodríguez Fernández, D.P. Rojas, J. Gutiérrez, P. Lázpita, I. Orue, Magnetic and magnetocaloric properties of martensitic Ni₂Mn_{1.4}Sn_{0.6} Heusler alloy, *J. Magn. Mater.* 324 (2012) 3519–3523.
- [9] N.H. Duc, T.D. Thanh, N.H. Yen, P.T. Thanh, N.H. Dan, T.L. Phan, Magnetic properties and magnetocaloric effect in Ni_{0.5}Mn_{0.5–x}Sb_x alloys, *J. Korean Phys. Soc.* 60 (2012) 454–459.
- [10] P.O. Castillo-Villa, L. Mañosa, A. Planes, D.E. Soto-Parra, J.L. Sánchez-Llamazares, H. Flores-Zúñiga, C. Frontera, Elastocaloric and magnetocaloric effects in Ni–Mn–Sn(Cu) shape-memory alloy, *J. Appl. Phys.* 113 (2013) 053506.
- [11] B. Lu, P. Zhang, Y. Xu, W. Sun, J. Liu, Elastocaloric effect in Ni₄₅Mn_{36.4}In_{13.6}Co₅ metamagnetic shape memory alloys under mechanical cycling, *Mater. Lett.* 148 (2015) 110–113.
- [12] Y. Sutou, Y. Imano, N. Koeda, T. Omori, R. Kainuma, K. Ishida, K. Oikawa, Magnetic and martensitic transformations of NiMnX (X=In,Sn,Sb) ferromagnetic shape memory alloys, *Appl. Phys. Lett.* 85 (2004) 4358–4360.
- [13] T. Krenke, M. Acet, E.F. Wassermann, X. Moya, L. Mañosa, A. Planes, Martensitic transitions and the nature of ferromagnetism in the austenitic and martensitic states of Ni–Mn–Sn alloys, *Phys. Rev. B.* 72 (2005).
- [14] D.H. Wang, C.L. Zhang, H.C. Xuan, Z.D. Han, J.R. Zhang, S.L. Tang, B.X. Gu, Y.W. Du, The study of low-field positive and negative magnetic entropy changes in Ni₄₃Mn_{46–x}Cu_xSn₁₁ alloys, *J. Appl. Phys.* 102 (2007) 013909.
- [15] Z. Liu, Z. Wu, H. Yang, Y. Liu, W. Wang, X. Ma, G. Wu, Martensitic transformation and magnetic properties in ferromagnetic shape memory alloy Ni₄₃Mn₄₆Sn_{11–x}Si_x, *Intermetallics*. 19 (2011) 1605–1611.
- [16] R. Das, S. Sarma, A. Perumal, A. Srinivasan, Effect of Co and Cu substitution on the magnetic entropy change in Ni₄₆Mn₄₃Sn₁₁ alloy, *J. Appl. Phys.* 109 (2011) 07A901.
- [17] C. Jing, Z. Li, H.L. Zhang, J.P. Chen, Y.F. Qiao, S.X. Cao, J.C. Zhang, Martensitic transition and inverse magnetocaloric effect in Co doping Ni–Mn–Sn Heusler alloy, *Eur. Phys. J. B.* 67 (2009) 193–196.
- [18] T. Krenke, E. Duman, M. Acet, X. Moya, L. Mañosa, A. Planes, Effect of Co and Fe on the inverse magnetocaloric properties of Ni–Mn–Sn, *J. Appl. Phys.* 102 (2007) 033903.

- [19] E.C. Passamani, F. Xavier, E. Favre-Nicolin, C. Larica, A.Y. Takeuchi, I.L. Castro, J.R. Proveti, Magnetic properties of NiMn-based Heusler alloys influenced by Fe atoms replacing Mn, *J. Appl. Phys.* 105 (2009) 033919.
- [20] K. Fukushima, K. Sano, T. Kanomata, H. Nishihara, Y. Furutani, T. Shishido, W. Ito, R.Y. Umetsu, R. Kainuma, K. Oikawa, K. Ishida, Phase diagram of Fe-substituted Ni–Mn–Sn shape memory alloys, *Scr. Mater.* 61 (2009) 813–816.
- [21] Z. Wu, Z. Liu, H. Yang, Y. Liu, G. Wu, R.C. Woodward, Metallurgical origin of the effect of Fe doping on the martensitic and magnetic transformation behaviours of Ni₅₀Mn_{40-x}Sn₁₀Fe_x magnetic shape memory alloys, *Intermetallics*. 19 (2011) 445–452.
- [22] B. Hernando, J.L.S. Llamazares, J.D. Santos, L. Escoda, J.J. Suñol, R. Varga, D. Baldomir, D. Serantes, Thermal and magnetic field-induced martensite-austenite transition in Ni_{50.3}Mn_{35.3}Sn_{14.4} ribbons, *Appl. Phys. Lett.* 92 (2008) 042504.
- [23] B. Hernando, J.L.S. Llamazares, J.D. Santos, M.L. Sánchez, L. Escoda, J.J. Suñol, R. Varga, C. García, J. González, Grain oriented NiMnSn and NiMnIn Heusler alloys ribbons produced by melt spinning: Martensitic transformation and magnetic properties, *J. Magn. Magn. Mater.* 321 (2009) 763–768.
- [24] W. Wang, J. Yu, Q. Zhai, Z. Luo, H. Zheng, Origin of retarded martensitic transformation in Heusler Ni–Mn–Sn melt-spun ribbons, *Intermetallics*. 42 (2013) 126–129.
- [25] V.V. Khovaylo, V.V. Rodionova, S.N. Shevyrtalov, V. Novosad, Magnetocaloric effect in “reduced” dimensions: Thin films, ribbons, and microwires of Heusler alloys and related compounds, *Phys. Stat. Sol. (b)*. 251 (2014) 2104–2113.
- [26] A. Yan, K.H. Müller, O. Gutfleisch, Structure and magnetic entropy change of melt-spun LaFe₁₁.57Si₁.43 ribbons, *J. Appl. Phys.* 97 (2005) 6102.
- [27] P.J. Ibarra-Gaytan, C.F. Sánchez-Valdes, J.L.S. Llamazares, P. Álvarez-Alonso, P. Gorria, J.A. Blanco, Texture-induced enhancement of the magnetocaloric response in melt-spun DyNi₂ ribbons, *Appl. Phys. Lett.* 103 (2013) 152401.
- [28] C.F. Sánchez-Valdés, J.L. Sánchez Llamazares, H. Flores-Zúñiga, D. Ríos-Jara, P. Alvarez-Alonso, P. Gorria, Magnetocaloric effect in melt-spun MnCoGe ribbons, *Scr. Mater.* 69 (2013) 211–214.
- [29] J. Rodríguez-Carvajal, Recent advances in magnetic structure determination by neutron powder diffraction, *Phys. B Condens. Matter*. 192 (1993) 55–69.
- [30] B.M. Wang, Y. Liu, B. Xia, P. Ren, L. Wang, Large exchange bias obtainable through zero-field cooling from an unmagnetized state in Ni–Mn–Sn alloys, *J. Appl. Phys.* 111 (2012) 043912.
- [31] P. Lázpita, V.A. Chernenko, J.M. Barandiarán, I. Orue, J. Gutiérrez, J. Feuchtwanger, J.A. Rodríguez-Velamazán, Influence of Magnetic Field on Magnetostructural Transition in Ni_{46.4}Mn_{32.8}Sn_{20.8} Heusler Alloy, *Mater. Sci. Forum*. 635 (2009) 89–95.
- [32] J.D. Santos, T. Sanchez, P. Alvarez, M.L. Sanchez, J.L.S. Llamazares, B. Hernando, L. Escoda, J.J. Suñol, R. Varga, Microstructure and magnetic properties of Ni₅₀Mn₃₇Sn₁₃ Heusler alloy ribbons, *J. Appl. Phys.* 103 (2008) 07B326.
- [33] H.C. Xuan, Q.Q. Cao, C.L. Zhang, S.C. Ma, S.Y. Chen, D.H. Wang, Y.W. Du, Large exchange bias field in the Ni–Mn–Sn Heusler alloys with high content of Mn, *Appl. Phys. Lett.* 96 (2010) 202502.
- [34] X.G. Zhao, M. Tong, C.W. Shih, B. Li, W.C. Chang, W. Liu, Z.D. Zhang, Microstructure, martensitic transitions, magnetocaloric, and exchange bias properties in Fe-doped Ni–Mn–Sn melt-spun ribbons, *J. Appl. Phys.* 113 (2013) 17A913.
- [35] K.H.J. Buschow, *Handbook of Magnetic Materials*, vol. 11, 1st ed., Elsevier BV, Amsterdam u.a., 2011.
- [36] V.A. Chernenko, Compositional instability of β -phase in Ni–Mn–Ga alloys, *Scr. Mater.* 40 (1999) 523–527.

- [37] B. Cordero, V. Gómez, A. E. Platero-Prats, M. Revés, J. Echeverría, E. Cremades, F. Barragán, S. Alvarez, Covalent radii revisited, *Dalton Trans.* 0 (2008) 2832–2838.
- [38] P. Entel, A. Dannenberg, M. Siewert, H.C. Herper, M.E. Gruner, V. Buchelnikov, V.A. Chernenko, Composition-Dependent Basics of Smart Heusler Materials from First- Principles Calculations, *Mater. Sci. Forum.* 684 (2011) 1–29.
- [39] T. Kanomata, K. Shirakawa, T. Kaneko, Effect of hydrostatic pressure on the Curie temperature of the Heusler alloys Ni₂MnZ (Z = Al, Ga, In, Sn and Sb), *J. Magn. Magn. Mater.* 65 (1987) 76–82.
- [40] V.V. Kokorin, V. Chernenko, Martensitic transformation in ferromagnetic Heusler alloy, *Fiz. Met. Metalloved.* 68 (1989) 1157–1161.
- [41] R. Kainuma, K. Oikawa, W. Ito, Y. Sutou, T. Kanomata, K. Ishida, Metamagnetic shape memory effect in NiMn-based Heusler-type alloys, *J. Mater. Chem.* 18 (2008) 1837–1842.
- [42] K.G. Sandeman, Magnetocaloric materials: The search for new systems, *Scr. Mater.* 67 (2012) 566–571.
- [43] K.A. Gschneidner Jr., V.K. Pecharsky, A.O. Pecharsky, C.B. Zimm, Recent Developments in Magnetic Refrigeration, *Mater. Sci. Forum.* 315-317 (1999) 69–76.
- [44] S. Kustov, M.L. Corró, J. Pons, E. Cesari, Entropy change and effect of magnetic field on martensitic transformation in a metamagnetic Ni–Co–Mn–In shape memory alloy, *Appl. Phys. Lett.* 94 (2009) 191901.
- [45] V. Recarte, J.I. Pérez-Landazábal, V. Sánchez-Alarcos, V. Zablotskii, E. Cesari, S. Kustov, Entropy change linked to the martensitic transformation in metamagnetic shape memory alloys, *Acta Mater.* 60 (2012) 3168–3175.
- [46] V.A. Chernenko, V.A. L'vov, E. Cesari, A. Kosogor, J.M. Barandiaran, Transformation Volume Effects on Shape Memory Alloys, *Metals.* 3 (2013) 237–282.
- [47] J.M. Barandiaran, V.A. Chernenko, E. Cesari, D. Salas, P. Lazpita, J. Gutierrez, I. Orue, Magnetic influence on the martensitic transformation entropy in Ni-Mn-In metamagnetic alloy, *Appl. Phys. Lett.* 102 (2013) 071904.

TABLE CAPTIONS

Table 1: Actual chemical compositions, valence electron concentration, and characteristic temperatures (from DSC), average enthalpies, and change of volume (from the linear fit of the empirical data) of MT, as well as the Curie temperatures of martensitic and austenitic phases (from the low-field thermomagnetization dependences) for $\text{Ni}_{50-x}\text{Fe}_x\text{Mn}_{40}\text{Sn}_{10}$ MetaMSMAs.

FIGURE CAPTIONS

Fig. 1. Micrographs of the $\text{Ni}_{50.3}\text{Mn}_{39.7}\text{Sn}_{9.9}$ ribbons surface for the ternary alloy (a) and for $\text{Ni}_{48.5}\text{Mn}_{39.5}\text{Sn}_{9.8}\text{Fe}_{2.2}$ (b) with corresponding cross-sectional views shown in the *insets*.

Fig. 2. DSC curves (a) and temperature dependences of the electric resistance (b) for $\text{Ni}_{50-x}\text{Fe}_x\text{Mn}_{40}\text{Sn}_{10}$ as-spun ribbons with different content of Fe. Lines are guides for the eyes.

Fig. 3. Diffraction patterns of the $\text{Ni}_{48.5}\text{Mn}_{39.5}\text{Sn}_{9.8}\text{Fe}_{2.2}$ as-spun ribbon below and above the MT temperature and their fit to the calculated cubic (a) and orthorhombic crystal structures (b) respectively. Temperature evolution of the X-ray diffraction patterns across MT exhibited by the same ribbon (c).

Fig. 4. Temperature dependence of the lattice parameters of martensite and austenite for each ribbon. Lines are guides for the eyes.

Fig. 5. Zero-field and field cooling mass magnetization curves measured at low applied magnetic field (5 mT) for the $\text{Ni}_{50-x}\text{Fe}_x\text{Mn}_{40}\text{Sn}_{10}$ as-spun ribbons. *Insets* show zooms in the vicinity of the MT temperatures and one magnetization dependence measured at 0.5 T for alloy with $x = 0$ (see the bottom panel). Temperatures T_C^M and T_B are attributed to the Curie temperature of martensite and blocking temperature respectively.

Fig. 6. Thermomagnetization curves for the $\text{Ni}_{50-x}\text{Fe}_x\text{Mn}_{40}\text{Sn}_{10}$ as-spun ribbons measured during heating process at four values of the applied magnetic field.

Fig. 7. Temperature-dependent volume of the unit cells for the austenitic and martensitic crystal lattices calculated using data from Fig.2. The schematic of the transformation volume determination is shown. Lines correspond to data linear fits.

Fig. 8. (a) Influence of Fe content on both the entropy change and volume effect at MT exhibiting by $\text{Ni}_{50-x}\text{Fe}_x\text{Mn}_{40}\text{Sn}_{10}$ ribbons; (b) Phase diagram of the martensitic and magnetic transitions in the

ribbons where FM and PM stand for the ferromagnetic and paramagnetic states respectively. T_C^A , T_C^M and $T_0 = (T_A+T_M)/2$ are the Curie temperatures of austenite, martensite and equilibrium MT temperature respectively. Lines are guides for the eyes.

Fig. 9. (a) Temperature dependence of the magnetic entropy change under different applied magnetic fields for $\text{Ni}_{50-x}\text{Fe}_x\text{Mn}_{40}\text{Sn}_{10}$ ($x = 2, 4, 6, 8$) ribbons; (b) Magnetic field dependence of the entropy change maximums associated with the structural and magnetic transitions; (c) Martensitic transformation temperature as a function of magnetic field for different compositions. The slope values are indicated. Dotted-lines correspond to the linear fitting of the data.

Fig. 10. Magnetic field dependence of the relative cooling power, RCP, calculated for the inverse (main graph) and conventional (inset) magnetocaloric effects exhibited by $\text{Ni}_{50-x}\text{Fe}_x\text{Mn}_{40}\text{Sn}_{10}$ ribbons.

Fig. 11. Total entropy at the martensitic transformation, ΔS , as a function of the generalized order parameter ($T_C^A - T_0$). Dotted line represents an exponential fit.

Table 1: Actual chemical compositions, valence electron concentration, and characteristic temperatures (from DSC), average enthalpies, and change of volume (from the linear fit of the empirical data) at MT, as well as the Curie temperatures of martensitic and austenitic phases (from the low-field thermomagnetization dependences) for $\text{Ni}_{50-x}\text{Fe}_x\text{Mn}_{40}\text{Sn}_{10}$ MetaMSMAs.

x	Actual Chemical Composition	e/a	T_{MS} (K)	T_{MF} (K)	T_{AS} (K)	T_{AF} (K)	$ \Delta H $ (J/g)	$(\Delta V/V)_{\text{fit}}$ (%)	T_{C}^{M} (K)	T_{C}^{A} (K)
0	$\text{Ni}_{50.3}\text{Mn}_{39.7}\text{Sn}_{9.9}$	8.21	425	408	423	438	16.5	1.1	185	444
2	$\text{Ni}_{48.5}\text{Mn}_{39.5}\text{Sn}_{9.8}\text{Fe}_{2.2}$	8.18	375	358	377	386	14.4	1.1	176	393
4	$\text{Ni}_{46.6}\text{Mn}_{39.4}\text{Sn}_{9.9}\text{Fe}_{4.0}$	8.14	356	340	356	367	14.0	1.2	174	369
6	$\text{Ni}_{45.2}\text{Mn}_{38.6}\text{Sn}_{9.9}\text{Fe}_{6.3}$	8.12	310	297	309	322	13.2	1.3	181	322
8	$\text{Ni}_{42.6}\text{Mn}_{39.6}\text{Sn}_{9.7}\text{Fe}_{8.1}$	8.07	285	267	286	299	12.9	1.4	171	287

Fig. 1. Micrographs of the $\text{Ni}_{50.3}\text{Mn}_{39.7}\text{Sn}_{9.9}$ ribbons surface for the ternary alloy (a) and for $\text{Ni}_{48.5}\text{Mn}_{39.5}\text{Sn}_{9.8}\text{Fe}_{2.2}$ (b) with corresponding cross-sectional views shown in the insets.

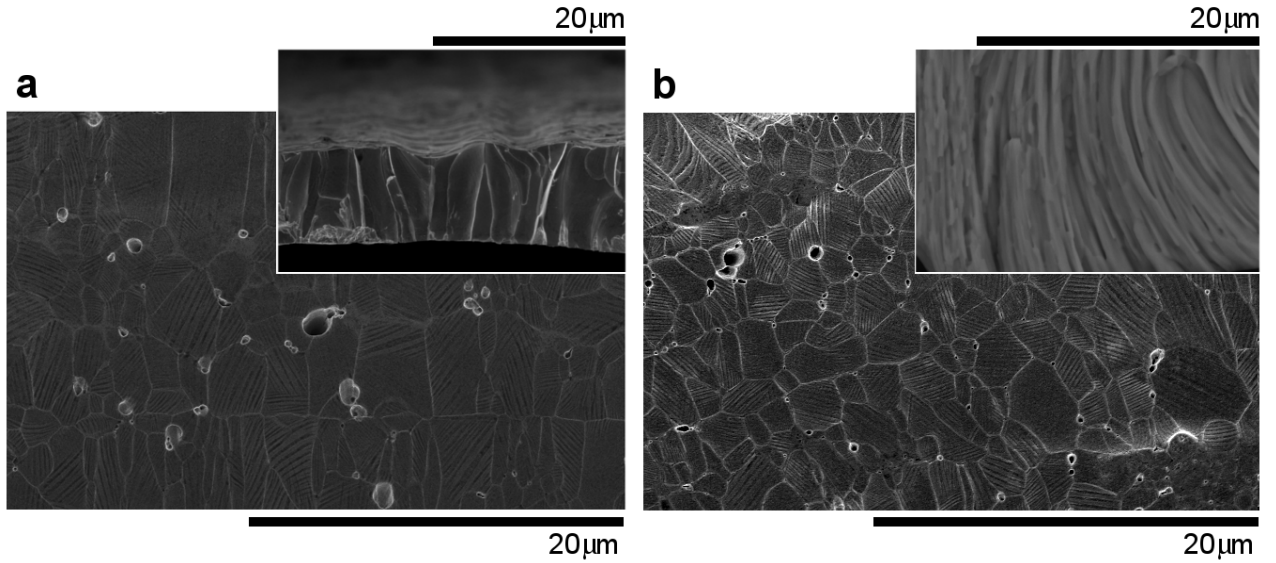


Fig. 2. DSC curves (a) and temperature dependences of the electric resistance (b) for $\text{Ni}_{50-x}\text{Fe}_x\text{Mn}_{40}\text{Sn}_{10}$ as-spun ribbons with a different content of Fe. Lines are guides for the eyes.

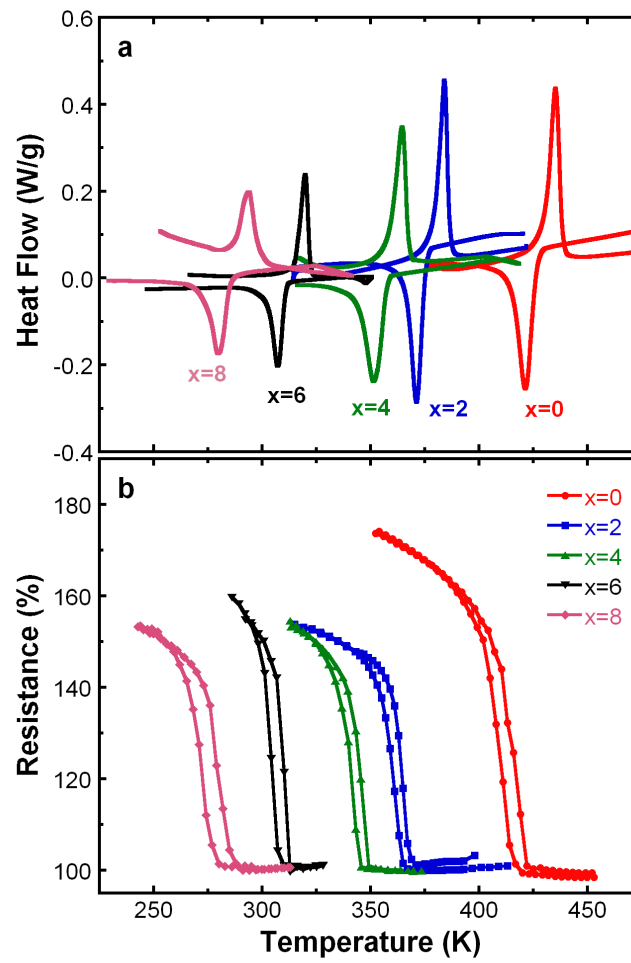


Fig. 3. Diffraction patterns of the $\text{Ni}_{48.5}\text{Mn}_{39.5}\text{Sn}_{9.8}\text{Fe}_{2.2}$ as-spun ribbon below and above the MT temperature and their fit to the calculated cubic (a) and orthorhombic crystal structures (b) respectively. Temperature evolution of the X-ray diffraction patterns across MT exhibited by the same ribbon (c).

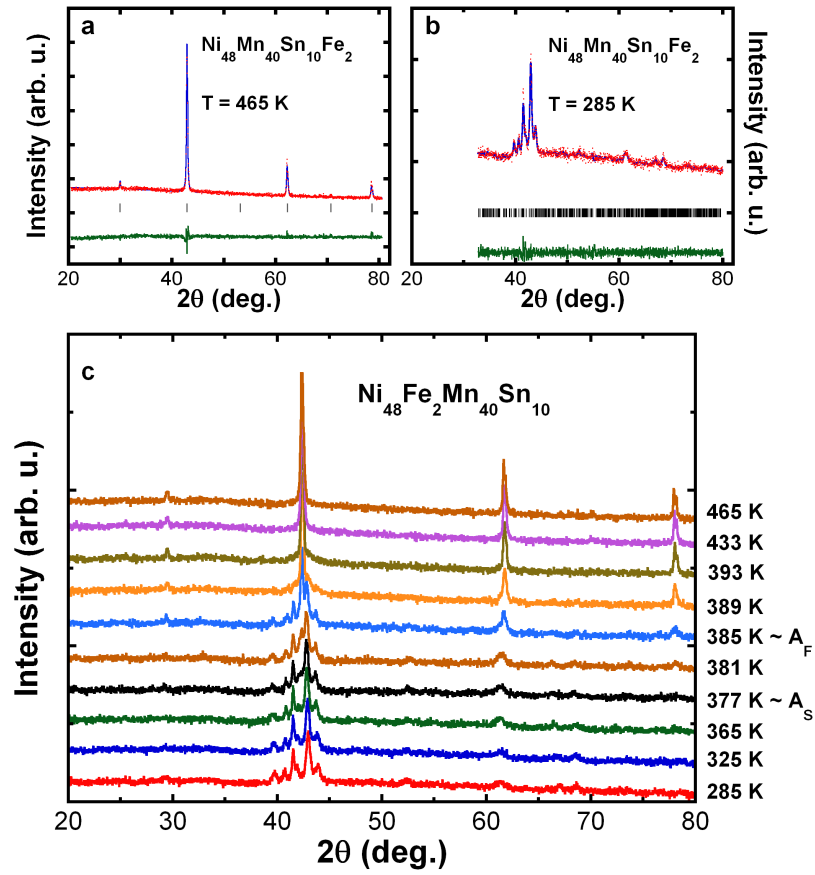


Fig. 4. Temperature dependences of the lattice parameters of martensite and austenite for each ribbon. Lines are guides for the eyes.

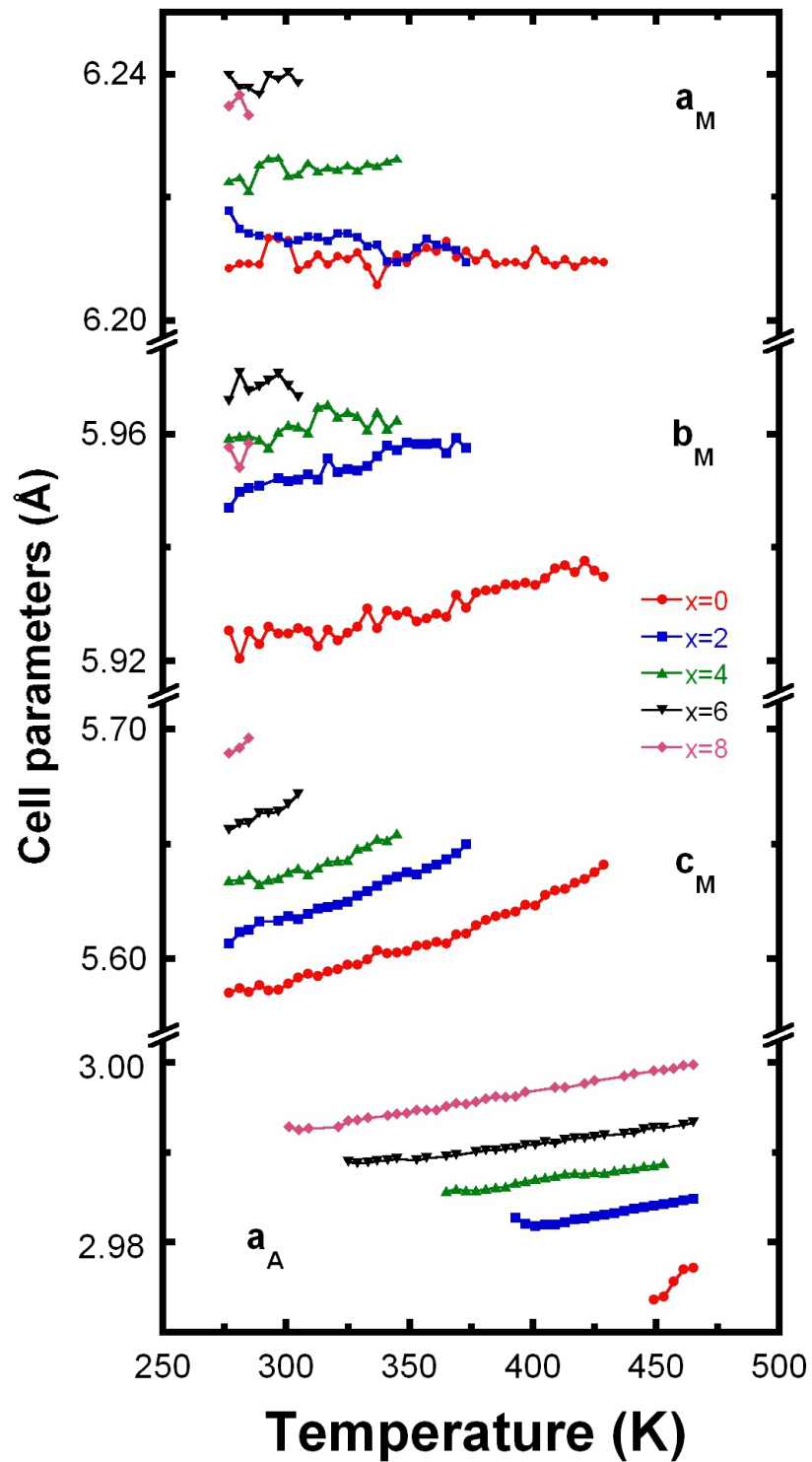


Fig. 5. Zero-field and field cooling magnetization curves measured at low applied magnetic field (5 mT) for the $\text{Ni}_{50-x}\text{Fe}_x\text{Mn}_{40}\text{Sn}_{10}$ as-spun ribbons. Insets show zooms in the vicinity of the MT temperatures and one magnetization dependence measured at 0.5 T for alloy with $x = 0$ (see the bottom panel). Temperatures T_C^M and T_B are attributed to the Curie temperature of martensite and blocking temperature, respectively.

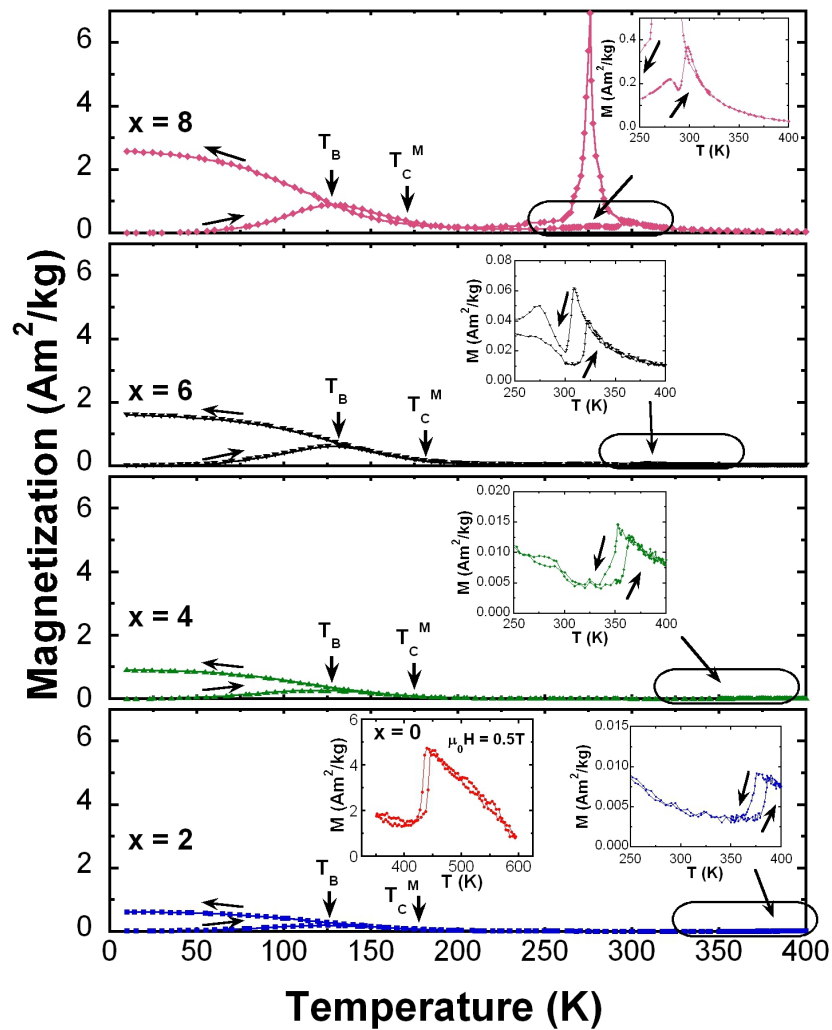


Fig. 6. Thermomagnetization curves for the $\text{Ni}_{50-x}\text{Fe}_x\text{Mn}_{40}\text{Sn}_{10}$ as-spun ribbons measured during heating process at four values of the applied magnetic field.

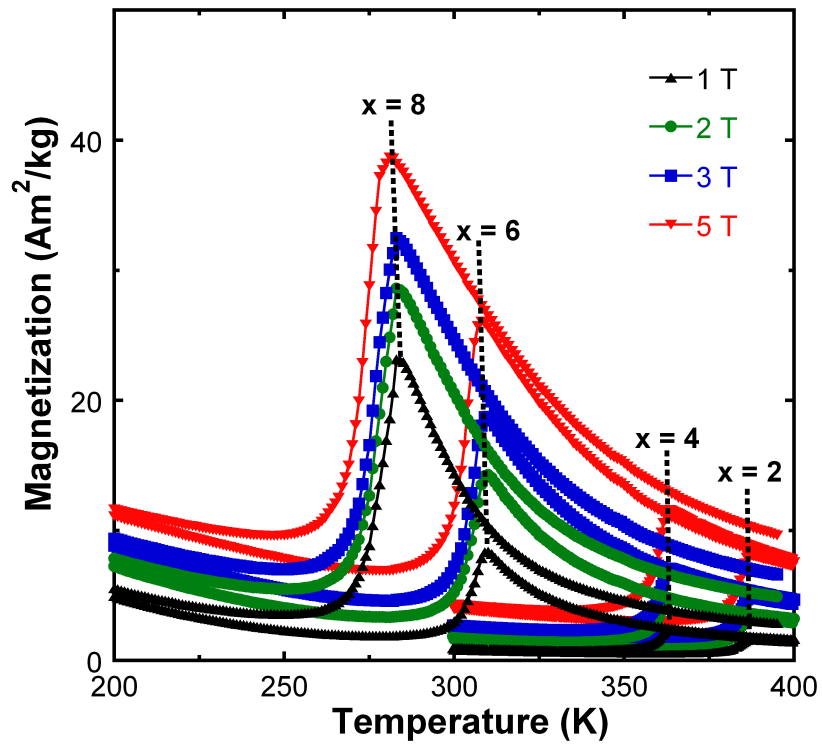


Fig. 7. Temperature-dependent volume of the unit cells for the austenitic and martensitic crystal lattices calculated using data from Fig.2. The schematic of the transformation volume determination is shown. Lines correspond to data linear fits.

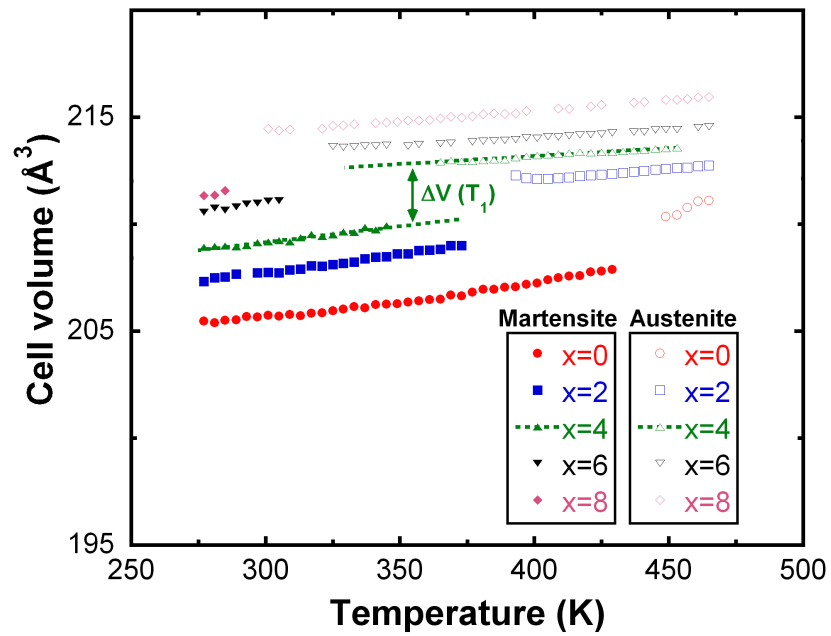


Fig. 8: (a) Influence of Fe content on both the entropy change and volume effect at MT exhibited by $\text{Ni}_{50-x}\text{Fe}_x\text{Mn}_{40}\text{Sn}_{10}$ ribbons; (b) Phase diagram of the martensitic and magnetic transitions in the ribbons where FM and PM stand for the ferromagnetic and paramagnetic states respectively. T_C^A , T_C^M and $T_0 = (T_A+T_M)/2$ are the Curie temperatures of austenite, martensite and equilibrium MT temperature respectively. Lines are guides for the eyes.

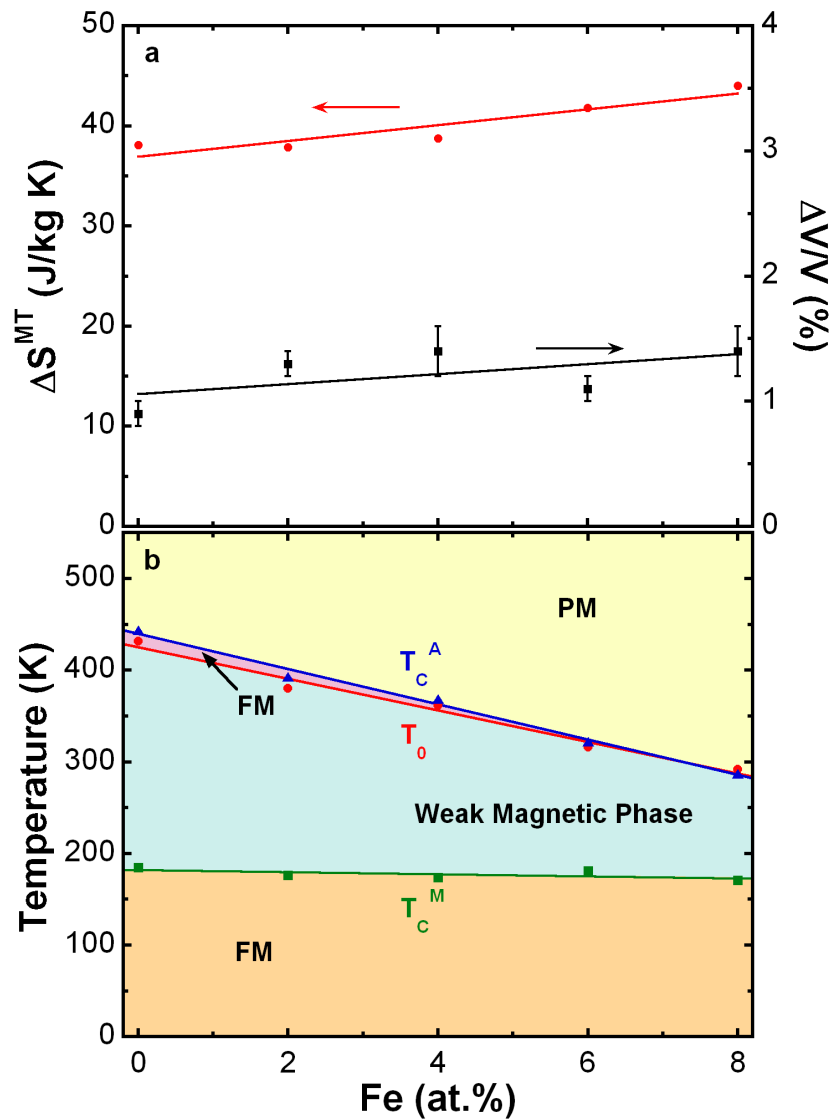


Fig. 9: (a) Temperature dependence of the magnetic entropy change under different applied magnetic fields for $\text{Ni}_{150-x}\text{Fe}_x\text{Mn}_{40}\text{Sn}_{10}$ ($x = 2, 4, 6, 8$) ribbons; (b) Magnetic field dependence of the entropy change maximums associated with the structural and magnetic transitions; (c) Martensitic transformation temperature as a function of magnetic field for different compositions. The slope values are indicated. Dotted-lines correspond to the linear fitting of the data.

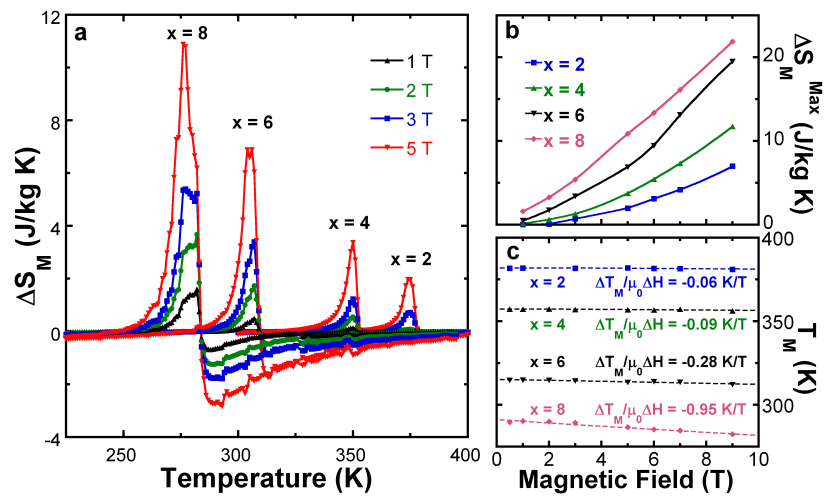


Fig. 10. Magnetic field dependence of the relative cooling power, RCP, calculated for the inverse (main graph) and conventional (inset) magnetocaloric effects exhibited by $\text{Ni}_{50-x}\text{Fe}_x\text{Mn}_{40}\text{Sn}_{10}$ ribbons.

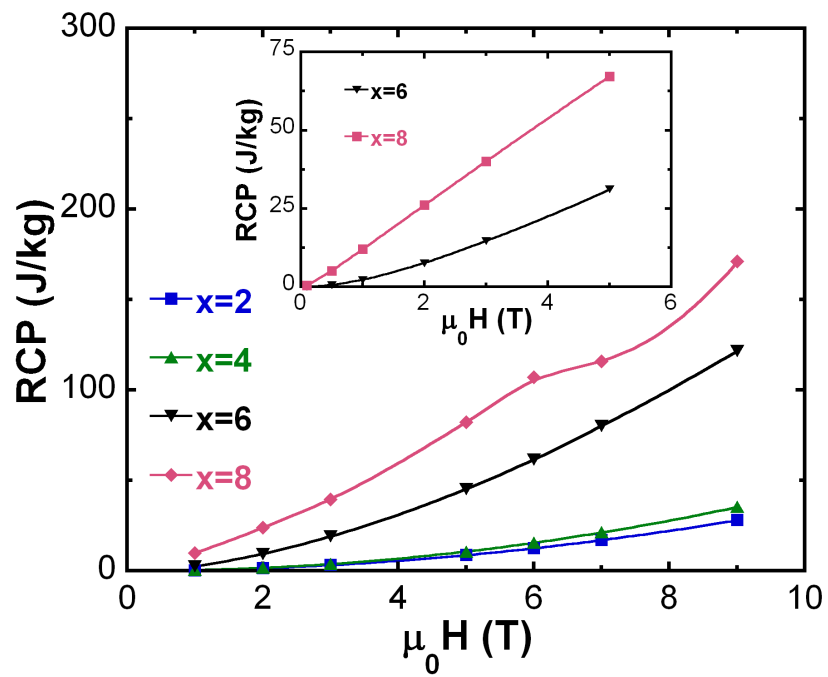


Fig. 11. Total entropy at the martensitic transformation, ΔS^{MT} , as a function of the generalized order parameter ($T_C^A - T_0$). Dotted line represents an exponential fit.

